Model Predictive Control of Dual-Mode Operations Z-Source Inverter: Islanded and Grid-Connected

Sally Sajadian, *Student Member, IEEE*, and Reza Ahmadi, *Member, IEEE*

***Abstract*—This paper presents model predictive control of dual-mode Z-source inverters (ZSIs) with capability to operate in islanded and grid-connected mode. The transition from islanded to grid-connected mode and vice versa can cause significant deviation in voltage and current due to mismatch in phase, frequency, and amplitude of voltages. The proposed controller offers seamless transition between the two modes of operations. The main predictive controller objectives are direct decoupled power control in grid-connected mode and load voltage regulation in islanded mode. The proposed direct decoupled active and reactive power control in grid-connected mode enables the dual-mode ZSI to behave as a power conditioning unit for ancillary services such as reactive power compensation. The proposed controller features simplicity, seamless transition between modes of operations, fast dynamic response, and small tracking error under steady-state condition of controller objectives. The operation of the proposed system is verified experimentally.**

***Index Terms*—Impedance-source inverter, maximum power point tracking (MPPT), model predictive control (MPC), photovoltaic (PV) systems.**

I. Introduction

CONVENTIONAL power systems are made-up of large central power plants that supply the loads through the transmission and distribution system. However, due to the recent increasing interest in exploiting renewable energy resources, the distributed generation (DG) facilities that are interfaced directly to the distribution network (DN) are becoming more ubiquitous. Photovoltaic (PV) generation systems are one of the most widely adopted DG facilities that are frequently connected to DN. The existing DN was not initially built with a concern for high-level DG integration; thus, the recent trend is leading to degraded DN system performance, safety, and reliability. Some of the well-known concerns pertaining to integration of more DG into the grid are the power quality issues, islanding operation mode, protection issues, and increased fault currents [2]–[5].

Islanding refers to the condition in which a portion of the grid (e.g., a microgrid) becomes temporarily isolated from the main grid but remains energized by its own DG resources [6]. Islanding may occur accidentally or deliberately. Commonly during the grid-connected operation, the DG systems are not responsible for frequency or voltage regulation, rather they only inject power to the grid. However, when a microgrid is cut off from the main grid at the point of common coupling (PCC), each renewable electricity generator has to detect the islanding situation [7], [8], and attempt to regulate the frequency and voltage of the microgrid. Sudden reconnection of an islanded microgrid to the grid after a period of islanded operation can have detrimental effects on DN operation because of the differences between the microgrid's and main grid's frequency, phase, and amplitude of the voltages. Therefore, sophisticated power electronic interface circuitry and advanced control schemes are required for DG inverters to ensure a smooth transition from/to the islanding condition.

There are many works in the literature that look at the islanding operation of microgrids and the effects on the main grid. In this regard, Pedersen *et al.* have provided several mathematical approaches for islanding analysis of wind farms based on measured voltage [9]. Ropp *et al*. proposed an islanding detection method using phase criteria and nondetection zones for PV applications [10]. Woyte *et al*. investigated the safety issues concerning the grid-connected PV inverters in case of unintentional islanding [11]. Bloemink *et al.* proposed a robust control strategy for multisourced microgrid with islanding capability [12]. Eghtedarpour *et al*. investigated control strategy for hybrid ac/dc microgrids for islanding operation [13]. Other researchers have also proposed several protection strategies, supervisory controllers, and architectures to enhance the islanding operation and smooth reconnection of microgrids with DG [14]–[20].

Traditionally, voltage source inverters (VSIs) or current source inverters (CSIs) are used as power electronic interfaces between renewable energy sources and local loads in microgrids. However, recently a new converter topology denoted as the impedance-source converter [21] is developed for the same purpose which undermines the limitations of the conventional VSIs and CSIs. These new converters provide several advantages for a variety of applications. In particular, Z-source inverters (ZSIs) can step up/down the voltage freely and thus are very well suited for designing single-stage PV DG systems. Fig. 1 demonstrates a single-stage PV DG system built around a ZSI. The focus of this paper is to propose a reliable and efficient control strategy for a dual-mode operation ZSI for PV applications. The main features of the proposed system are: single loop multi-objective predictive controller with hybrid cost function and adaptive weight factors, robust operation under distorted grid voltage, decoupled active and reactive power control in grid-connected mode, seamless transition between islanded

Manuscript received March 14, 2017; revised May 14, 2017; accepted June 19, 2017. Date of publication July 4, 2017; date of current version February 1, 2018. Recommended for publication by Associate Editor Dmitri Vinnikov. *(Corresponding author: Reza Ahmadi.)*

The authors are with the Department of Electrical Engineering and Computer Science, University of Kansas, Lawrence, KS 66045 USA (e-mail: sally.sajadian@ku.edu; ahmadi@ku.edu).

Color versions of one or more of the figures in this paper are available online at http://ieeexplore.ieee.org.

Digital Object Identifier 10.1109/TPEL.2017.2723358

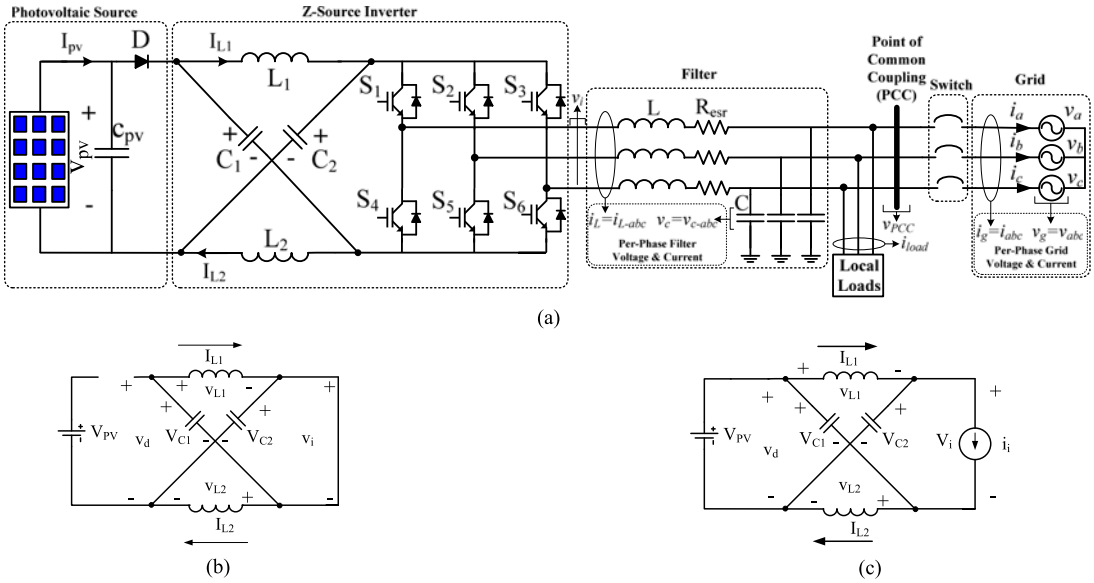

Fig. 1. (a) Dual-mode Z-source inverter, (b) the equivalent circuit of the impedance network of the ZSI during a shoot-through mode, and (c) a nonshoot-through mode.

and grid-connected modes of operation, voltage regulation in islanded mode, and reactive power compensation at PCC as an ancillary service from the DG system to the grid.

The transition between grid-connected and islanded operating modes may result in voltage spikes across the local loads, at PCC, leading to injection of inrush currents into the grid due to mismatch between frequency, phase, or amplitude of the voltages. Although several control methods have been proposed in the literature for dual-mode operating inverters with seamless transfer characteristics [22]–[25], most of these methods use multiple-loop cascaded controllers which are difficult to tune and implement, and may not have reliable operation under abnormalities in the grid such as distorted grid voltage. This paper uses the model predictive control (MPC) [26], [27] method to develop a new control strategy for dual-mode ZSIs with the capability to seamlessly transit between grid-connected and islanded modes of operation. The proposed methodology is solving only a single optimization problem for all operation modes. This feature simplifies the controller algorithm compared to linear multiloop classic controllers for dual-mode operation inverters. This advantage is particularly more important for impedance source inverters which require advance modulation scheme due to existence of shoot-through state in addition to active and null states.

This paper is structured as follows: Section II explains the structure of the proposed system and provides the details of the controller design for each mode of operations. Finally, it presents a strategy for islanding mode detection based on active frequency drift (AFD) method. Section III presents experimental results. Section IV concludes this paper.

II. Proposed Model Predictive Control of the System

A. System Description and Model

The modes of operation of the system can be classified to two steady-state modes and two transition modes. The steady-

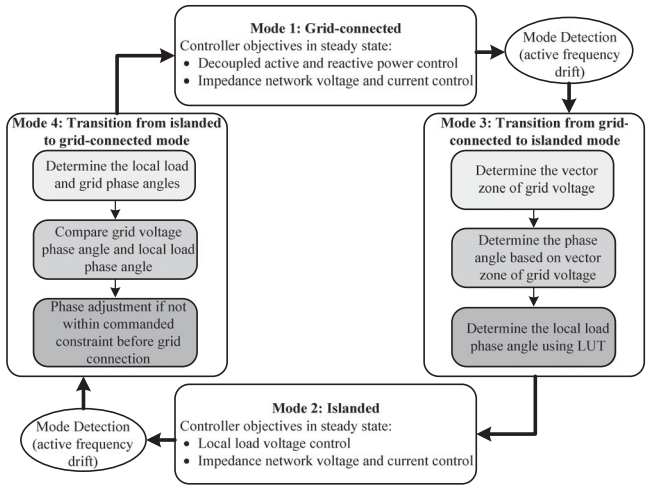

Fig. 2. Modes of operation of the proposed Z-source inverter.

state modes are the grid-connected and islanded modes. The transition modes are transition from the grid-connected mode to the islanded mode and vice versa. The state diagram for transition between the four modes of operation of system is illustrated in Fig. 2. As pictured, a decoupled active and reactive power controller that can freely adjust the power factor of the ZSI is proposed for the grid-connected mode. In the islanded mode the required local load voltage is regulated by the same controller but with different terms in the proposed MPC cost function. In both steady-state modes, the voltage and current of the impedance network are controlled to adjust the ZSI gain by operating in the shoot-through and nonshoot-through states, for applications such as the maximum power point tracking (MPPT) for the PV source. For transition modes, a grid-synchronization and phase adjustment algorithm is proposed to seamlessly transit from the grid-connected mode to the islanded mode and vice versa. Based on the application, the reference signals for

the MPC cost function are generated. For example, for the PV application, the reference active power is determined from the MPPT algorithm and the dc-link voltage control [28].

In this section, the derivation of the predictive model of the system will be discussed. In the stationary reference frame, the per-phase output filter dynamic model of the ZSI is given by the output filter inductor current and capacitor voltage:

$$\frac{d}{dt}i_L(t) = \frac{1}{L}(v_i(t) - v_{\text{PCC}}(t) - i_L(t)R_{\text{esr}}) \tag{1}$$

$$\frac{d}{dt}v_C(t) = \frac{d}{dt}v_{\text{PCC}}(t) = \frac{1}{C}(i_L(t) - i_{\text{Load}}(t)) \tag{2}$$

where $i_L(t)$ is the filter inductor current, $v_i(t)$ is the output voltage before the filter, $v_{\text{PCC}}(t)$ is the voltage at the PCC, L is the grid side inductance of the filter, and R_{esr} is the equivalent series resistance of the inductor. Using the Euler forward method, (1) and (2) can be approximated using

$$\frac{dx(t)}{dt} \approx \frac{\tilde{x}(k+1) - x(k)}{T_S} \tag{3}$$

where T_s is the sampling period and k is discretized t. The predicted inductor current $\tilde{i}_L(k+1)$ and capacitor voltage $\tilde{v}_C(k+1)$ can be found from (1) to (3) as

$$\tilde{i}_L(k+1) = \frac{T_s}{L}(v_i(k) - v_{\text{PCC}}(k) - i_L(k)R_{\text{esr}}) + i_L(k) \tag{4}$$

$$\tilde{v}_C(k+1) = \frac{T_s}{C}i_C(k+1) + v_C(k). \tag{5}$$

Moreover, the grid side voltage (v_g) can be predicted at time $(k+1)$ using

$$\tilde{v}_g(k+1) = v_g(k)e^{j\omega T_S} \tag{6}$$

where ωT_s is the amount of change in angle of the grid side voltage over one sampling interval T_s, for a grid voltage with angular frequency of ω. If the sampling interval is sufficiently small, it can be approximated that $\tilde{v}_g(k+1) \approx v_g(k)$. Additionally, from (2) and the Euler forward approximation, the predicted value of the per-phase local load current in islanded mode can be formulated by

$$\tilde{i}_{\text{Load}}(k+1) = i_L(k+1) - \frac{C}{T_s}(v_c(k+1) - v_c(k)). \tag{7}$$

A distinctive characteristic of a ZSI is its capability to leverage shoot-through switching states for boosting the output voltage. In shoot-through states both switches in one leg of the inverter are turned ON simultaneously. Fig. 1(b) and (c) illustrates the equivalent circuits of the impedance-network of the ZSI shown in Fig. 1(a) during the shoot-through and nonshoot-through modes. At the PV side, the discretized equations for a nonshoot-through state are found in the literature as [29], [30]

$$\begin{cases} \tilde{I}_{L1}(k+1) = I_{L1}(k) + \dfrac{T_S}{L_1}(V_{\text{pv}} - V_{C1}(k) - R_{L1}I_{L1}(k)) \\ \tilde{V}_{C1}(k+1) = V_{C1}(k) + \dfrac{T_S}{C_1}(\tilde{I}_{L1}(k+1) - \tilde{I}_{\text{inv}}(k+1)) \end{cases} \tag{8}$$

where

$$\tilde{I}_{\text{inv}}(k+1) = S_1 \times I_a(k) + S_2 \times I_b(k) + S_3 \times I_c(k). \tag{9}$$

The discretized equations for the shoot-through state are found similarly from [29], [30]

$$\begin{cases} \tilde{I}_{L1}(k+1) = I_{L1}(k) + \dfrac{T_S}{L_1}(V_{C1}(k) - R_{L1}I_{L1}(k)) \\ \tilde{V}_{C1}(k+1) = V_{C1}(k) - \dfrac{T_S}{C_1}I_{L1}(k+1) \end{cases}. \tag{10}$$

B. Grid-Connected and Islanded Model

In the grid connected mode, the proposed controller for the ZSI behaves as a current regulator by injecting power to the grid. The controller objectives in this mode of operation are decoupled active and reactive power control as well as the voltage and current control for the impedance network elements. The dual-mode operation ZSI system can operate with adjustable power factor, enabled by the proposed decoupled power control.

Most of the robust grid synchronization techniques available in the literature require multiple cascaded control loops that need to be designed and tuned. Commonly, the grid synchronization requires the amplitude and phase angle information of the grid voltage detected by the phase-locked loop [31], [32]. Also, some other synchronization subsystems are usually needed for conventional grid-connected inverter system including synchronization reference frame [33], [34]. These multiloop cascaded control loop adds design complexity, adverse transient performance, and even system instability [35], [36]. Therefore, second-order generalized integrator (SOGI) which is a simple synchronization algorithm with proved harmonic distortion rejection capability is used in this paper for generation of orthogonal α-β phase components for the ZSI. The characteristic transfer functions of SOGI in S-domain are given by [37]

$$\frac{x_\alpha(s)}{x(s)} = \frac{\chi\omega s}{s^2 + \chi\omega s + \omega^2} \tag{11}$$

$$\frac{x_\beta(s)}{x(s)} = \frac{\chi\omega^2}{s^2 + \chi\omega s + \omega^2} \tag{12}$$

where χ is the damping factor and ω is the fundamental frequency. The SOGI can filter the harmonics that are far from the fundamental frequency. The SOGI can effectively extract the fundamental component from signals with all harmonic components.

In order to determine the predictive active and reactive power model for MPC, by using the SOGI, the orthogonal $\alpha - \beta$ phase components of PCC voltage v_{PCC} and current i_L are generated and given by

$$v_{\text{PCC}-\alpha} = V_m \sin(\omega t) \tag{13}$$

$$v_{\text{PCC}-\beta} = -V_m \cos(\omega t) \tag{14}$$

$$i_{L-\alpha} = I_m \sin(\omega t - \phi) \tag{15}$$

$$i_{L-\beta} = -I_m \cos(\omega t - \phi). \tag{16}$$

Accordingly, the active and reactive power in $\alpha-\beta$ can be formulated as [38]

$$x=\begin{bmatrix}P\\Q\end{bmatrix}=\frac{3}{2}\begin{bmatrix}v_{\text{PCC}-\alpha} & v_{\text{PCC}-\beta}\\ v_{\text{PCC}-\beta} & -v_{\text{PCC}-\alpha}\end{bmatrix}\begin{bmatrix}i_{L-\alpha}\\ i_{L-\beta}\end{bmatrix}. \tag{17}$$

Then, the derivative of active and reactive power with respect to time can be found as

$$\begin{bmatrix}\frac{dP}{dt}\\ \frac{dQ}{dt}\end{bmatrix}=\frac{3}{2}\begin{bmatrix}\frac{dv_{\text{PCC}-\alpha}}{dt} & \frac{dv_{\text{PCC}-\beta}}{dt}\\ \frac{dv_{\text{PCC}-\beta}}{dt} & -\frac{dv_{\text{PCC}-\alpha}}{dt}\end{bmatrix}\begin{bmatrix}i_{L-\alpha}\\ i_{L-\beta}\end{bmatrix}+\frac{3}{2}\begin{bmatrix}v_{\text{PCC}-\alpha} & v_{\text{PCC}-\beta}\\ v_{\text{PCC}-\beta} & -v_{\text{PCC}-\alpha}\end{bmatrix}\begin{bmatrix}\frac{di_{L-\alpha}}{dt}\\ \frac{di_{L-\beta}}{dt}\end{bmatrix} \tag{18}$$

while the derivative of PCC voltages $v_{\text{PCC}-\alpha}$ and $v_{\text{PCC}-\beta}$ with respect to time can be found as

$$\begin{aligned}\frac{dv_{\text{PCC}-\alpha}}{dt}&=-\omega\times v_{\text{PCC}-\beta}\\ \frac{dv_{\text{PCC}-\beta}}{dt}&=\omega\times v_{\text{PCC}-\alpha}.\end{aligned} \tag{19}$$

The state-space model of the system with respect to active and reactive power can then be found from (17) to (19) and (1) as

$$\frac{dx}{dt}=Ax+Bv_i-Ev_{\text{PCC}} \tag{20}$$

where

$$x=\begin{bmatrix}P & Q\end{bmatrix}^T,\ B=\frac{3}{2L}\begin{bmatrix}v_{\text{PCC}-\alpha} & v_{\text{PCC}-\beta}\\ v_{\text{PCC}-\beta} & -v_{\text{PCC}-\alpha}\end{bmatrix},$$

$$A=\begin{bmatrix}-\frac{R_{\text{esr}}}{L} & -\omega\\ \omega & -\frac{R_{esr}}{L}\end{bmatrix},\ E=\frac{3}{2L}\begin{bmatrix}v_{\text{PCC}-\alpha} & v_{\text{PCC}-\beta}\\ 0 & 0\end{bmatrix}. \tag{21}$$

Thus, the system is presented in state-space format with *P* and *Q* as the state variables. In (20), v_i is the input and v_{PCC} is a measured value. Using the Euler forward method, the discrete-time model of (20) can be found as

$$\tilde{x}(k+1)=x(k)+T_s\left(Ax(k)+Bv_i(k)-Ev_{\text{PCC}}(k)\right). \tag{22}$$

This equation can be used to formulate the predicted active and reactive power at instant $(k+1)$

$$\begin{aligned}\tilde{P}(k+1)&=P(k)-\omega T_sQ(k)\\ &\quad+\frac{3T_s}{2L}\left(V_m^2-v_{\text{PCC}-\alpha}(k)v_{i-\alpha}(k)-v_{\text{PCC}-\beta}(k)v_{i-\beta}(k)\right)\\ \tilde{Q}(k+1)&=Q(k)+\omega T_sP(k)\\ &\quad-\frac{3T_s}{2L}\left(v_{\text{PCC}-\beta}(k)v_{i-\alpha}(k)-v_{\text{PCC}-\alpha}(k)v_{i-\beta}(k)\right).\end{aligned} \tag{23}$$

Thus, two of the control variables (active and reactive power) for grid-connected mode of operation can be predicted measuring the filter inductor current i_L (grid side current in grid-connected mode), the PCC voltage v_{PCC}, and the inverter output voltage v_i, all in two-axis stationary reference frame $\alpha-\beta$. The other two control variables, i.e., inductor current (I_{L1}) and capacitor voltage (V_{C1}) on the PV side, are predicted using (8) and (10).

In the islanded mode of operation, the ZSI is disconnected from the grid at the PCC. The ZSI will supply the local loads in this mode. The controller objectives are to regulate the voltage across the local loads by using (5) and to control the impedance network current and voltages using (8) and (10).

C. Transition Modes: Grid Synchronization and Phase Adjustment

According to the state diagram of Fig. 2, during the two transition modes the proposed grid synchronization and phase adjustment method will be triggered to ensure seamless transition. The block diagram of the proposed grid synchronization and phase adjustment method is illustrated in Fig. 3. The input to the grid synchronization algorithm is the peak grid voltage (V_g) and α component of the grid voltage $(v_{g-\alpha})$ which is generated using the SOGI module. The low-pass filter characteristics of the SOGI modules filter out the grid voltage harmonics to obtain the fundamental component phase information of the grid voltage. The algorithm starts by estimating the grid voltage phase using

$$\hat{\phi}_g=\sin^{-1}\left(\left|\frac{v_{g-\alpha}(t)}{V_g}\right|\right). \tag{24}$$

Due to symmetry characteristic of the sinusoidal waveform, the phase angle given by (24) can correspond to two different magnitude over one cycle. Thus, an exact phase angle determination is required. A zonal detection approach is used to determine the exact phase angle that corresponds to specific voltage magnitude according to (24). As illustrated in Fig. 4, a sinusoidal waveform can be divided into four zones in one cycle. A look-up table with saved values of a sine function is used; four zones are identified over a sinusoidal cycle as illustrated in Fig. 4 in order to get the appropriate point in look-up table with the right phase angle information of the grid voltage. The vector zone of grid voltage and as a result the exact phase angle is determined using the $v_g(k)$ and $v_g(k-1)$ values as follows:

$$\begin{cases}v_g(k)>0\ \&\ v_g(k)>v_g(k-1)\Rightarrow\text{zone 1}\\ v_g(k)>0\ \&\ v_g(k)<v_g(k-1)\Rightarrow\text{zone 2}\\ v_g(k)<0\ \&\ v_g(k)<v_g(k-1)\Rightarrow\text{zone 3}\\ v_g(k)<0\ \&\ v_g(k)>v_g(k-1)\Rightarrow\text{zone 4}\end{cases} \tag{25}$$

$$\tilde{\phi}_g=\begin{cases}\phi_g & \text{zone 1}\\ \frac{360}{2}-\phi_g & \text{zone 2}\\ \frac{360}{2}+\phi_g & \text{zone 3}\\ 360-\phi_g & \text{zone 4}\end{cases} \tag{26}$$

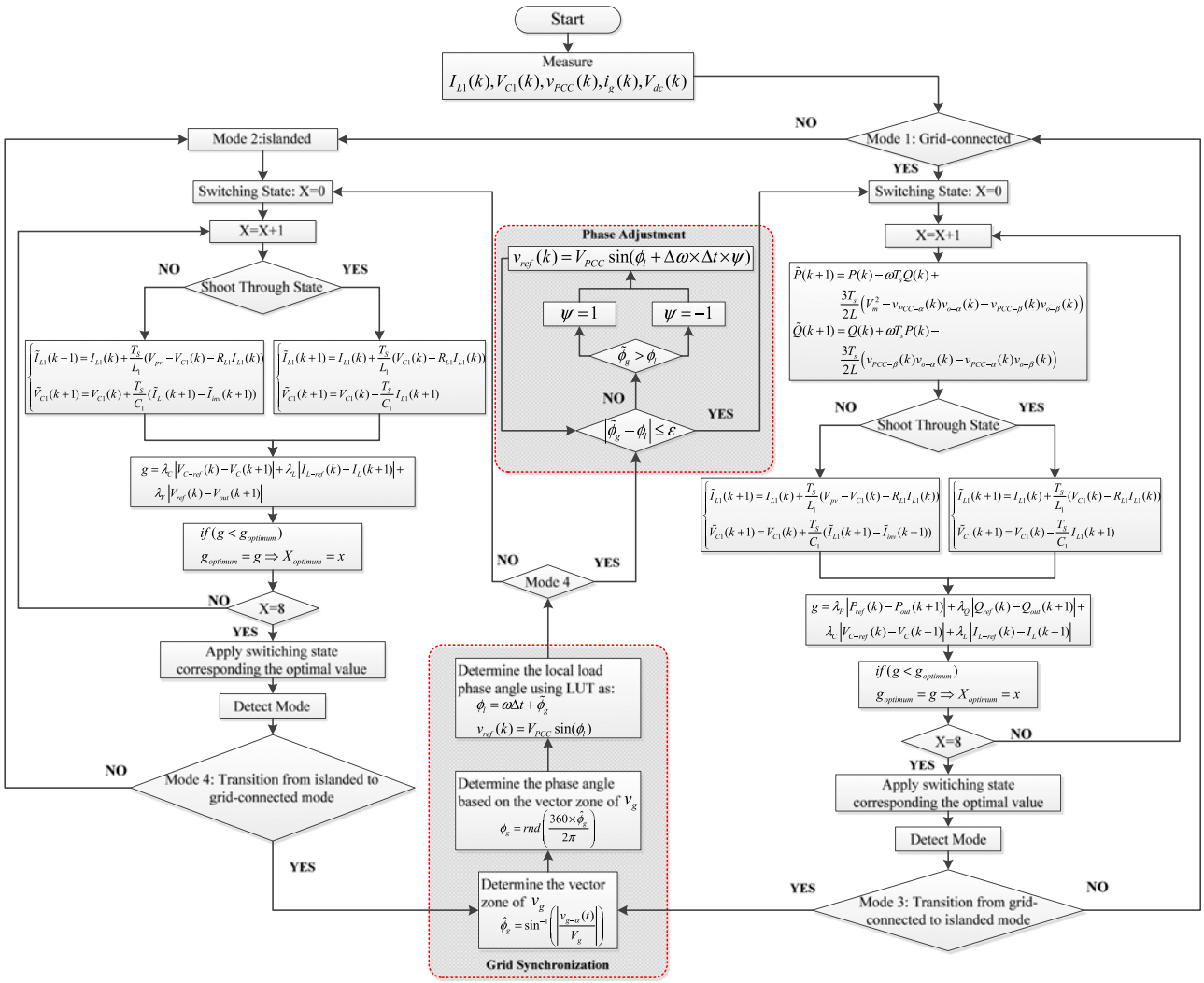

Fig. 3. Proposed model predictive control for Z-source inverter dual mode operation: grid-connected and islanded.

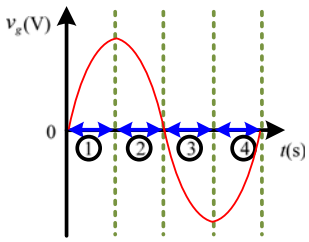

Fig. 4. Zonal representation of grid voltage.

where

$$\phi_g = \text{rnd}\left(\frac{360\times\hat{\phi}_g}{2\pi}\right). \tag{27}$$

Once the phase angle is determined according to (25)–(27), the reference voltage for the islanded mode of operation can be determined over the transition period by

$$\phi_l = \omega\Delta t + \tilde{\phi}_g$$
$$v_{\text{ref}}(k) = V_{\text{PCC}}\sin(\phi_l). \tag{28}$$

This grid synchronization is required for both transition modes (modes 1 and 2). In mode 2 (transition from islanded to grid-connected mode), a phase adjustment will be triggered after the grid voltage restauration. The phase adjustment algorithm evaluates the phase angle difference between the local load and the grid, if their difference is negligible (smaller than some predefined ε), then the phase angle information will be sent to grid-connected mode control algorithm. If the phase difference is bigger than ε, then a unit increment/decrement in the frequency is carried-out to adjust the phase difference for seamless transition from islanded mode to grid-connected mode. Thus, the reference voltage is determined as

$$v_{\text{ref}}(k) = V_{\text{PCC}}\sin(\phi_l + \Delta\omega\times\Delta t\times\psi) \tag{29}$$

where Ψ is 1 if $\tilde{\phi}_g > \phi_l$ and -1 if $\tilde{\phi}_g < \phi_l$, after each increment/decrement in the phase angle. The phase difference $(|\tilde{\phi}_g - \phi_l|)$ is evaluated until the absolute value of the phase angle difference between the grid voltage and the local load voltage is smaller than ε.

D. Controller Formulation and Algorithm

As mentioned earlier, there are four modes of operation for the proposed controller of dual-mode inverter: two steady-state modes and two transition modes. The objective of two transition modes is to ensure synchronization and seamless transfer. The summary of the controller algorithm is illustrated in Fig. 3. In this paper, a single cost function subject to minimization for all modes of operation is developed; the whole optimization problem for the system is formulated as follows:

$$\min g = \begin{cases} \lambda_P g_P + \lambda_Q g_Q + \lambda_C g_C + \lambda_L g_L & \text{for modes 1, 3, 4} \\ \lambda'_C g_C + \lambda'_L g_L + \lambda'_V g_V & \text{for mode 2} \end{cases}$$

subject to

$$\tilde{x}(k+1) = x(k) + T_S(Ax(k) + Bu(k))$$
$$g_P = |P_{\text{ref}}(k) - P_{\text{out}}(k+1)|, g_Q = |Q_{\text{ref}}(k) - Q_{\text{out}}(k+1)|$$
$$g_C = |V_{C-\text{ref}}(k) - V_C(k+1)|, g_L = |I_{L-\text{ref}}(k) - I_L(k+1)|$$
$$g_V = |V_{\text{ref}}(k) - V_i(k+1)|. \quad (30)$$

The weight factors $(\lambda_P, \lambda_Q, \lambda_C, \lambda_L)$ are selected adaptively based on the modes of operation. According to (30), two set of $(\lambda_P, \lambda_Q, \lambda_C, \lambda_L)$ coefficient are selected: one set for modes 1, 3, 4 and another set for mode 2. The weights factors are determined using branch and bound technique [26], tracking errors of each control objectives and injected grid current total harmonic distortion (THD) are used as a tool for selection of weight factors using branch and bound technique.

Assuming the system is operating initially in mode 1, at the end of the control algorithm for mode 1, the mode detection algorithm determines the ZSI mode of operation. If mode 2 is detected, the grid synchronization algorithm will be triggered to determine the reference voltage for local loads to be regulated in mode 2. As illustrated in Fig. 3, mode 2 also regulates the C_1 voltage and L_1 current for determination of shoot-through and nonshoot-through operation. Then the optimization problem of (30) will be executed for mode 2. The voltage vector that minimizes the cost function will be determined and applied to the converter in mode 2. The mode detection algorithm runs again at the end of each loop. If mode 1 is detected, the grid synchronization and phase adjustment algorithms will be triggered to seamlessly transit to grid-connected mode.

E. Mode of Operation Detection Algorithm

Islanding detection is a required feature in control of dual mode grid-connected inverters. The islanded mode of operation may occur intentionally and unintentionally. Unintentional islanding occurs when there is a fault at the main grid and the ZSI is disconnected from the grid, only supplying the local loads. The intentional islanding also can happen by a command to the controller for only supplying the local loads. For either situation, the proposed controller first operates in mode 3 (transition mode) and then switches to mode 2. Thus, in order to have a seamless transfer, an islanding detection technique is required for unintentional islanding mode.

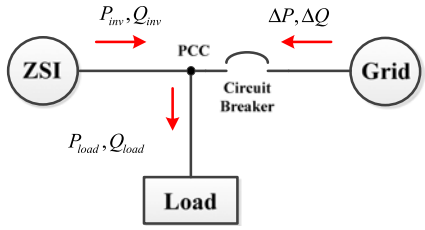

Fig. 5. One-line-network diagram at the point of common coupling (PCC).

Several islanding mode detections have been reported in the literature [12], [39], [40]. AFD method [39], [41] has received considerable attention for PV DG systems because of its simplicity and easy implementation. In this paper AFD is used for islanding mode detection. This section provides a brief review of the AFD technique.

An attractive solution for implementation of AFD is the attempt to drift the frequency or the magnitude of the PCC voltage beyond the allowed normal range of the parameters that are known as standard under- and over-frequency protection and under- and over-voltage protection [39]. An equivalent network of the ZSI, local loads, and the grid at PCC is shown in Fig. 5. The active and reactive powers being consumed by the local loads (assuming *RLC* load) are given by

$$P_{\text{load}} = \frac{3V_{\text{PCC}}^2}{R} = P_{\text{inv}} \quad (31)$$

$$Q_{\text{load}} = \frac{3V_{\text{PCC}}^2}{X_C}\left[\left(\frac{f_0}{f_{\text{PCC}}}\right)^2 - 1\right] = Q_{\text{inv}} \quad (32)$$

where f_0 and f_{PCC} are the resonant frequency of the load and PCC frequency in islanding mode of operation. Equation (31) can be used to find

$$V_{\text{PCC}} = \sqrt{\frac{1}{3}P_{\text{inv}}R}. \quad (33)$$

Thus, in islanding mode, the voltage at PCC is a function of active power of the ZSI. If the harvested PV power does not match the required power by the load, V_{PCC} must increase/decrease to match the load power and the PV power. Thus, in the islanded mode, voltage drifting is achieved by varying P_{inv}. From (33), it can be seen that V_{PCC} is a function of P_{inv} and R only; thus, the frequency can be drifted by changing Q_{inv} as given by (32). Thus, the frequency of current follows the frequency of voltage at mode 1 because of the direct power control in this mode. In mode 2, depending on the reactive power control reference for the proposed controller, the value of the PCC voltage frequency tends to drift downward/upward. As an example, if the PV system was operating with unity power factor $(Q_{\text{ref}}(k) = 0)$, the frequency of PCC voltage would tend to drift downward. The detail procedure is provided in [39] and [41].

III. Results and Discussions

The proposed controller is implemented in MATLAB/Simulink and experimentally validated using the PLECS RT Box. The experimental setup for this system is shown in

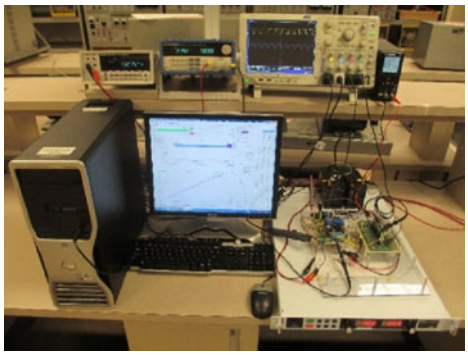

Fig. 6. Experimental setup.

TABLE I
SYSTEM PARAMETERS [1]

Parameter	Value
C_1	1000 μF
C_2	1000 μF
L_1	0.7 mH
L_2	0.7 mH
Sampling time	60 μs
C_{pv}	470 μF
L_{grid}	1 mH
V_{PCC}	120 V
Local load case 1	30 Ω
Local load case 2	60 Ω

Fig. 6. The detail system parameters are given in Table I, the ZSI components design strategy are available in [1] . The proposed system is experimentally tested for several case studies in the grid-connected mode and islanded mode. The performance of the proposed controller is evaluated by looking into four important merit criteria: seamless transition between grid-connected mode and islanded mode, phase adjustment and grid synchronization, seamless transition between grid-connected and islanded mode with different frequencies, decoupled active and reactive power control in grid-connected mode, fast dynamic response of active and reactive power due to change in solar irradiance level or change in reactive power required by the grid at PCC, low tracking error in steady-state operation, and reliable operation under distorted grid voltage in grid-connected mode.

The transitions from grid-connected mode to islanded mode and vice versa are first examined. The v_{PCC}, i_L, and i_g waveforms for this transition are shown in the scope shots of Figs. 7 and 8. As pictured in Fig. 7, the dual-mode ZSI is initially connected to the grid and then it is disconnected from the grid. After disconnection from the grid, the grid current i_g goes to zero instantly. The dual-mode ZSI operates in islanded mode after a short period for islanding detection and transition. It can be seen that a seamless transition from grid-connected to islanded mode is achieved without overshoot/undershoot for PCC voltage v_{PCC} and/or inductor current i_L during this transition process. In order to demonstrate the flexibility and reliability of the proposed controller, the local loads in islanded mode are assumed to operate at 180 Hz instead of 60 Hz grid frequency. This case study demonstrates the capability of the proposed system to

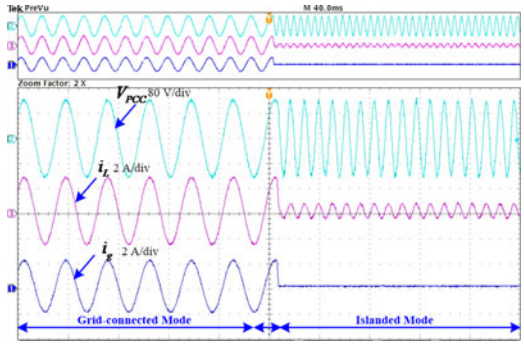

Fig. 7. Seamless transition from grid-connected to islanded mode.

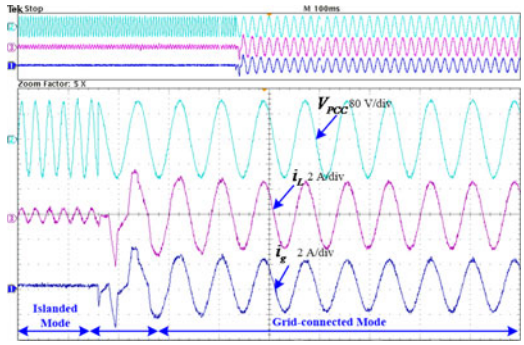

Fig. 8. Seamless transition from islanded mode to grid-connected mode.

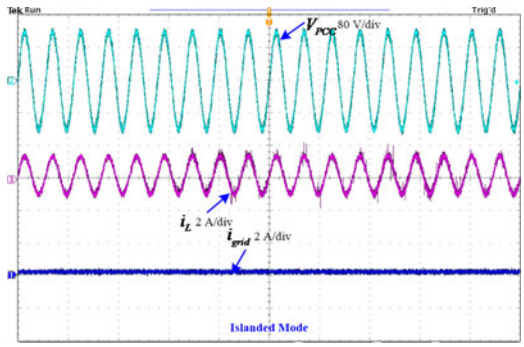

Fig. 9. Islanded mode of operation.

seamlessly transfer to islanded mode while the local load frequency is different than the grid frequency.

Fig. 8 demonstrates the dual-mode ZSI performance for transition from islanded mode to grid-connected mode. As picture, the ZSI is initially supplying local loads when islanded, then it will go to transition mode when the grid is ready to reconnect and the grid synchronization as well as phase adjustment algorithms are triggered. Similar to previous case, the transition happened seamlessly without harsh dynamic behavior in v_{PCC}, i_L, and i_g as shown in Fig. 8.

The experimental results of the dual-mode ZSI operation in islanded mode and grid-connected mode are shown in Figs. 9–11. A resistive load of 60 Ω is considered as the local load for islanded operation of the system in Fig. 9, the v_{PCC}, i_L, and i_g waveforms are shown in Fig. 9 for this experiment. As it is pictured, the load voltage is tracking its reference PCC voltage for this case study with peak voltage of 120 V.

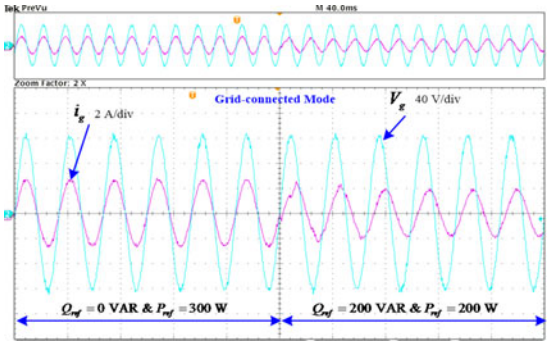

Fig. 10. Grid-connected mode: step change in active and reactive reference power, the reactive power changed from 0 to 200 VAR and the active power is changed from 300 to 200 W.

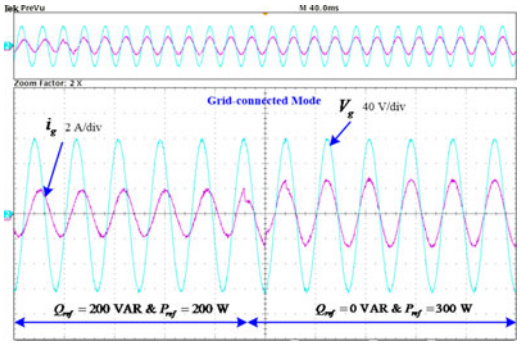

Fig. 11. Grid connected mode: step change in active and reactive reference power, the reactive power changed from 200 to 0 VAR and the active reference power is changed from 200 to 300 W.

TABLE II
HARMONICS DISTORTION OF GRID-SIDE CURRENT

Harmonic Order	Distortion (%)
3rd	0.94%
5th	0.03%
7th	0.54%
9th	0.14%
11th	0.28%
13th	0.22%
15th	0.14%
17th	0.11%

Figs. 10 and 11 show the grid-connected mode operation when a step change is applied to active and reactive power references. In Fig. 10, the active and reactive power references are initially 300 W and 0 VAR (unity power factor), respectively, then a step change is applied to the active and reactive power references. The reactive power is changed to 200 VAR and active power is decreased to 200 W. In Fig. 11, the active and reactive powers are changed back to 300 W and 0 VAR. As it is shown in Figs. 10 and 11, the grid current overshoot/undershoot is negligible. The active and reactive power tracking errors are less than 0.06%. In order to evaluate the quality of the injected current to the grid, the individual harmonic components of the grid side current i_g are tabulated in Table II, the calculated i_g THD of 2.48% is within the IEEE-519 standards for grid-tied systems [42]. Figs. 12 and 13 show the three phase inductor

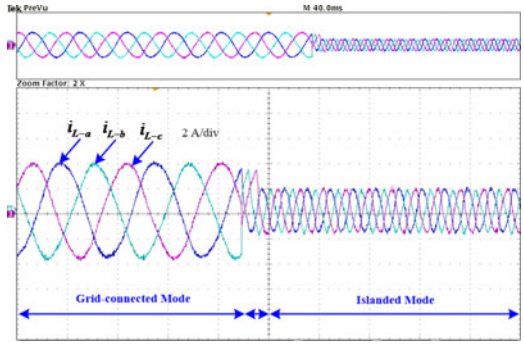

Fig. 12. Waveform of i_{L-abc} during seamless transition from grid-connected mode to islanded mode for local load of 30 Ω.

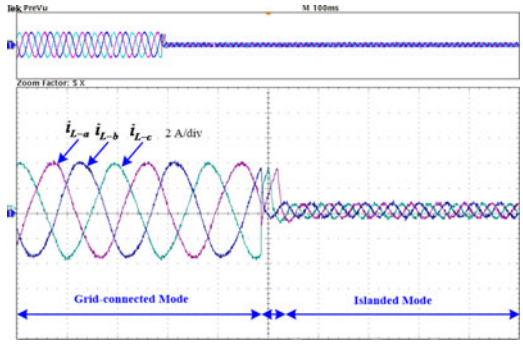

Fig. 13. Waveform of i_{L-abc} during seamless transition from grid-connected mode to islanded mode for local load of 60 Ω.

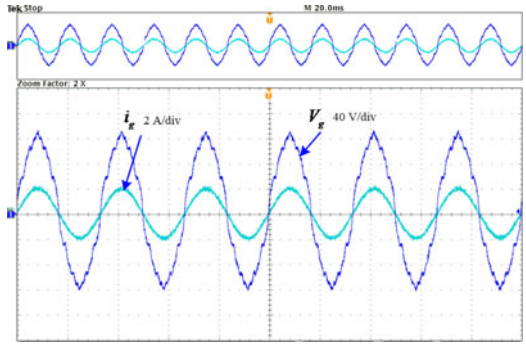

Fig. 14. Waveform of i_g and v_g under distorted grid voltage.

(i_{L-abc})—current during seamless transition for resistive local load of 30 and 60 Ω. As it is pictured, for both cases of local load connected at the PCC to the system, seamless transition is achieved without significant deviation in the current.

Fig. 14 shows the performance of the proposed controller under distorted grid voltage (v_g) in grid-connected mode. As shown in Fig. 14, the grid current is not affected by the distorted grid voltage. The commanded unity power factor operation with high quality current waveform is achieved. Fig. 15 shows the experimental dynamic performance of active and reactive power to big step change in active and reactive power references. A step change is applied to active power from 200 to 800 W and in reactive power from 500 to 0 VAR. As pictured in Fig. 15, the reference of active and reactive power was initially 200 W and 500 VAR, respectively; then, at time 2 s, a step change is applied to active and reactive power from 200 to 800 W and from 500 to

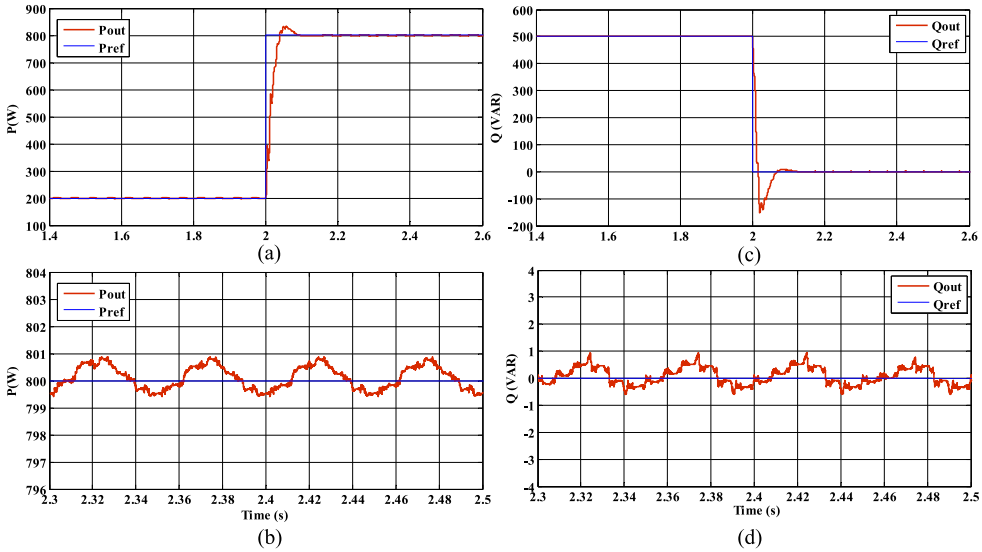

Fig. 15. Experimental results active and reactive power tracking: (a) active power tracking response to step change from 200 to 800 W, (b) active power steady-state tracking error, (c) reactive power tracking response to step change from 500 to 0 VAR, and (d) reactive power steady-state tracking error.

0 VAR, respectively. As shown, the results demonstrate promising dynamic response for such a big step change also. The steady-state operation tracking errors are shown in Fig. 15(b) and (d), as it is pictured the power ripple is negligible. The active power tracking error is negligible with active power ripple of less than 0.8 W peak to peak. Similarly, the reactive power is tracked with negligible oscillation and tracking error, for unity power factor reference, the achieved experimental power factor is around 0.99 and the reactive power ripple is less than 0.8 VAR peak to peak. It worth mentioning that for the proposed multi-objective control system, priorities can be given to individual control objectives by adjusting the weight factors in the MPC cost function (30). The active and reactive power tracking performance in Fig. 15 can be adjusted by lowering the tracking accuracy of other control objectives in (30) from their references.

Thus an engineering trade-off is applied in this paper to balance the tracking performance between all the control objectives in the single hybrid cost function of (30).

IV. Conclusion

This paper proposes a MPC technique for a dual-mode ZSI with seamless transition between grid-connection and islanding mode without significant deviation in voltage and current due to mismatch in phase, frequency, and amplitude of grid voltage and load. The proposed single loop controller determines the optimal switching states for the ZSI based on its mode of operation. A single hybrid cost function is developed for all modes of operation which simplifies the design and practical implementation of the proposed model based predictive controller. This characteristic of the proposed system is well suited for the impedance source inverters which require advance and complex modulation scheme due to their shoot-through state in addition to active and null states. The hybrid cost function is optimized during each sampling time to: harvest the maximum power from the PV module, inject the active power to the grid, provide reactive power compensation for the grid as an ancillary service to the grid through PCC, and maintain the PCC voltage in the islanded mode. The explanation of system modes of operation, strategy to transit between modes of operation, and operation in steady-state modes are provided. Several experimental case studies are provided to validate the theoretical expectations. The results demonstrate robust operation in all modes of operation. The main features of the proposed controller are high quality grid current in grid connected mode, fast dynamic response in grid-connected mode to step change in active and reactive power, negligible power ripple in steady-state operation, seamless transition between modes of operation without significant deviation in PCC voltage and current, robust operation under distorted grid voltage, and capability to operate at different frequencies in islanded mode of operation.

References

[1] H. Abu-Rub, Y. Liu, B. Ge, F. Blaabjerg, O. Ellabban, and P. C. Loh, *Impedance Source Power Electronic Converters*. Hoboken, NJ, USA: Wiley, 2016.

[2] S. A. Saleh, A. S. Aljankawey, E. Ozkop, and R. Meng, "On the experimental performance of a coordinated antiislanding protection for systems with multiple DGUs," *IEEE Trans. Power Electron.*, vol. 32, no. 2, pp. 1106–1123, Feb. 2017.

[3] K. O. Oureilidis and C. S. Demoulias, "A fault clearing method in converter-dominated microgrids with conventional protection means," *IEEE Trans. Power Electron.*, vol. 31, no. 6, pp. 4628–4640, Jun. 2016.

[4] F. Liu, W. Liu, X. Zha, H. Yang, and K. Feng, "Solid-state circuit breaker snubber design for transient overvoltage suppression at bus fault interruption in low-voltage dc microgrid," *IEEE Trans. Power Electron.*, vol. 32, no. 4, pp. 3007–3021, Apr. 2017.

[5] H. T. Do, X. Zhang, N. V. Nguyen, S. S. Li, and T. T. T. Chu, "Passive-islanding detection method using the wavelet packet transform in grid-connected photovoltaic systems," *IEEE Trans. Power Electron.*, vol. 31, no. 10, pp. 6955–6967, Oct. 2016.

[6] C. Li, J. Savulak, and R. Reinmuller, "Unintentional islanding of distributed generation-operating experiences from naturally occurred events," *IEEE Trans. Power Del.*, vol. 29, no. 1, pp. 269–274, Feb. 2014.

[7] J. He, Y. W. Li, and F. Blaabjerg, "An enhanced islanding microgrid reactive power, imbalance power, and harmonic power sharing scheme," *IEEE Trans. Power Electron.*, vol. 30, no. 6, pp. 3389–3401, Jun. 2015.

[8] K. T. Tan, P. L. So, Y. C. Chu, and M. Z. Q. Chen, "Coordinated control and energy management of distributed generation inverters in a microgrid," *IEEE Trans. Power Del.*, vol. 28, no. 2, pp. 704–713, Apr. 2013.
[9] J. K. Pedersen, M. Akke, N. K. Poulsen, and K. O. H. Pedersen, "Analysis of wind farm islanding experiment," *IEEE Trans. Energy Convers.*, vol. 15, no. 1, pp. 110–115, Mar. 2000.
[10] M. E. Ropp, M. Begovic, A. Rohatgi, G. A. Kern, R. H. Bonn, and S. Gonzalez, "Determining the relative effectiveness of islanding detection methods using phase criteria and nondetection zones," *IEEE Trans. Energy Convers.*, vol. 15, no. 3, pp. 290–296, Sep. 2000.
[11] A. Woyte, R. Belmans, and J. Nijs, "Testing the islanding protection function of photovoltaic inverters," *IEEE Trans. Energy Convers.*, vol. 15, no. 3, pp. 290–296, Sep. 2000.
[12] J. M. Bloemink and M. R. Iravani, "Control of a multiple source microgrid with built-in islanding detection and current limiting," *IEEE Trans. Power Del.*, vol. 27, no. 4, pp. 2122–2132, Oct. 2012.
[13] N. Eghtedarpour and E. Farjah, "Power control and management in a hybrid ac/dc microgrid," *IEEE Trans. Smart Grid*, vol. 5, no. 3, pp. 1494–1505, May 2014.
[14] T. V. Tran, T. W. Chun, H. H. Lee, H. G. Kim, and E. C. Nho, "PLL-based seamless transfer control between grid-connected and islanding modes in grid-connected inverters," *IEEE Trans. Power Electron.*, vol. 29, no. 10, pp. 5218–5228, Oct. 2014.
[15] S. Moayedi and A. Davoudi, "Unifying distributed dynamic optimization and control of islanded dc microgrids," *IEEE Trans. Power Electron.*, vol. 32, no. 3, pp. 2329–2346, Mar. 2017.
[16] A. Bidram, V. Nasirian, A. Davoudi, and F. L. Lewis, "Control and modeling of microgrids," in *Cooperative Synchronization in Distributed Microgrid Control*. New York, NY, USA: Springer, 2017, pp. 7–43.
[17] W. R. Issa, M. A. Abusara, and S. M. Sharkh, "Control of transient power during unintentional islanding of microgrids," *IEEE Trans. Power Electron.*, vol. 30, no. 8, pp. 4573–4584, Aug. 2015.
[18] L. G. Meegahapola, D. Robinson, A. P. Agalgaonkar, S. Perera, and P. Ciufo, "Microgrids of commercial buildings: Strategies to manage mode transfer from grid connected to islanded mode," *IEEE Trans. Sustain. Energy*, vol. 5, no. 4, pp. 1337–1347, Oct. 2014.
[19] D. Dong *et al.*, "Modes of operation and system-level control of single-phase bidirectional PWM converter for microgrid systems," *IEEE Trans. Smart Grid*, vol. 3, no. 1, pp. 93–104, Mar. 2012.
[20] G. Hernandez-Gonzalez and R. Iravani, "Current injection for active islanding detection of electronically-interfaced distributed resources," *IEEE Trans. Power Del.*, vol. 21, no. 3, pp. 1698–1705, Jul. 2006.
[21] P. Fang Zheng, "Z-source inverter," *IEEE Trans. Ind. Appl.*, vol. 39, no. 2, pp. 504–510, Mar./Apr. 2003.
[22] D. S. Ochs, B. Mirafzal, and P. Sotoodeh, "A method of seamless transitions between grid-tied and stand-alone modes of operation for utility-interactive three-phase inverters," *IEEE Trans. Ind. Appl.*, vol. 50, no. 3, pp. 1934–1941, May/Jun. 2014.
[23] Q.-C. Zhong and T. Hornik, "Cascaded current–voltage control to improve the power quality for a grid-connected inverter with a local load," *IEEE Trans. Ind. Electron.*, vol. 60, no. 4, pp. 1344–1355, Apr. 2013.
[24] Z. Yao, L. Xiao, and Y. Yan, "Seamless transfer of single-phase grid-interactive inverters between grid-connected and stand-alone modes," *IEEE Trans. Power Electron.*, vol. 25, no. 6, pp. 1597–1603, Jun. 2010.
[25] R.-J. Wai, C.-Y. Lin, Y.-C. Huang, and Y.-R. Chang, "Design of high-performance stand-alone and grid-connected inverter for distributed generation applications," *IEEE Trans. Ind. Electron.*, vol. 60, no. 4, pp. 1542–1555, Apr. 2013.
[26] J. Rodriguez *et al.*, "State of the art of finite control set model predictive control in power electronics," *IEEE Trans. Ind. Informat.*, vol. 9, no. 2, pp. 1003–1016, May 2013.
[27] B. Stellato, T. Geyer, and P. J. Goulart, "High-speed finite control set model predictive control for power electronics," *IEEE Trans. Power Electron.*, vol. 32, no. 5, pp. 4007–4020, May 2017.
[28] S. Sajadian and R. Ahmadi, "Model predictive based maximum power point tracking for grid-tied photovoltaic applications using a Z-source inverter," *IEEE Trans. Power Electron.*, vol. 31, no. 11, pp. 7611–7620, Nov. 2016.
[29] O. Ellabban, J. Van Mierlo, and P. Lataire, "A DSP-based dual-loop peak dc-link voltage control strategy of the Z-source inverter," *IEEE Trans. Power Electron.*, vol. 27, no. 9, pp. 4088–4097, Sep. 2012.
[30] L. Jingbo, H. Jiangang, and X. Longya, "Dynamic modeling and analysis of Z source converter-derivation of ac small signal model and design-oriented analysis," *IEEE Trans. Power Electron.*, vol. 22, no. 5, pp. 1786–1796, Sep. 2007.
[31] Z. Yao, L. Xiao, and J. M. Guerrero, "Improved control strategy for the three-phase grid-connected inverter," *IET Renew. Power Gener.*, vol. 9, pp. 587–592, 2015.
[32] M. Ciobotaru, V. G. Agelidis, R. Teodorescu, and F. Blaabjerg, "Accurate and less-disturbing active antiislanding method based on PLL for grid-connected converters," *IEEE Trans. Power Electron.*, vol. 25, no. 6, pp. 1576–1584, Jun. 2010.
[33] S. Dasgupta, S. K. Sahoo, and S. K. Panda, "Single-phase inverter control techniques for interfacing renewable energy sources with microgrid-Part I: Parallel-connected inverter topology with active and reactive power flow control along with grid current shaping," *IEEE Trans. Power Electron.*, vol. 26, no. 3, pp. 717–731, Mar. 2011.
[34] X. Q. Guo and W. Y. Wu, "Improved current regulation of three-phase grid-connected voltage-source inverters for distributed generation systems," *IET Renew. Power Gener.*, vol. 4, pp. 101–115, 2010.
[35] Z. Qing-Chang, N. Phi-Long, M. Zhenyu, and S. Wanxing, "Self-synchronized synchronverters: Inverters without a dedicated synchronization unit," *IEEE Trans. Power Electron.*, vol. 29, no. 2, pp. 617–630, Feb. 2014.
[36] Y. Yang, F. Blaabjerg, H. Wang, and M. G. Simoes, "Power control flexibilities for grid-connected multi-functional photovoltaic inverters," *IET Renew. Power Gener.*, vol. 10, pp. 504–513, 2016.
[37] F. Xiao, L. Dong, L. Li, and X. Liao, "A frequency-fixed SOGI-based PLL for single-phase grid-connected converters," *IEEE Trans. Power Electron.*, vol. 32, no. 3, pp. 1713–1719, Mar. 2017.
[38] E. Pouresmaeil, C. Miguel-Espinar, M. Massot-Campos, D. Montesinos-Miracle, and O. Gomis-Bellmunt, "A control technique for integration of DG units to the electrical networks," *IEEE Trans. Ind. Electron.*, vol. 60, no. 7, pp. 2881–2893, Jul. 2013.
[39] L. A. C. Lopes and S. Huili, "Performance assessment of active frequency drifting islanding detection methods," *IEEE Trans. Energy Convers.*, vol. 21, no. 1, pp. 171–180, Mar. 2006.
[40] J. Merino, P. Mendoza-Araya, G. Venkataramanan, and M. Baysal, "Islanding detection in microgrids using harmonic signatures," *IEEE Trans. Power Del.*, vol. 30, no. 5, pp. 2102–2109, Oct. 2015.
[41] L. A. C. Lopes and Y. Zhang, "Islanding detection assessment of multi-inverter systems with active frequency drifting methods," *IEEE Trans. Power Del.*, vol. 23, no. 1, pp. 480–486, Jan. 2008.
[42] IW Group, "IEEE recommended practices and requirements for harmonic control in electrical power systems," IEEE Std. 519-1992, 1992.

Sally Sajadian (S'14) received the B.S. and M.S. degrees in electrical engineering from the Purdue School of Engineering, Indianapolis, IN, USA, in 2012 and 2014, respectively. She is currently working toward the Ph.D. degree in the Department of Electrical Engineering and Computer Science, University of Kansas, Lawrence, KS, USA.

Her research interests include photovoltaic systems, renewable energy systems, power electronics, and control of power electronics interfaces.

Reza Ahmadi (M'09) received the B.S. degree from the Iran University of Science and Technology, Tehran, Iran, in 2009, and the Ph.D. degree from Missouri University of Science and Technology, Rolla, MO, USA, in 2013, both in electrical engineering.

He is currently an Assistant Professor of electrical engineering and computer science with the University of Kansas, Lawrence, KS, USA. His research interests include modeling, design, and control of power electronic converters, electric-drive vehicles, and solar energy systems.